Peer-reviewed version available at Nanomaterials 2019, 9, 1249; doi:10.3390/nano9091249

Structure-function correlations in sputter deposited gold/fluorocarbon multilayers for tuning optical response

Pallavi Pandit[1*], Matthias Schwartzkopf[1], André Rothkirch[1], Stephan V. Roth[1, 2], Sigrid Bernstorff[3] and Ajay Gupta[4*]

[1] Deutsches Elektronen-Synchrotron (DESY), Notkestraße 85, D-22607 Hamburg, Germany

[2]KTH Royal Institute of Technology, Department of Fibre and Polymer Technology, Teknikringen 56-58, SE-100 44 Stockholm, Sweden

[3]Elettra-Sincrotrone Trieste, SS 14, Km 163.5, I-34149 Basovizza, Trieste, Italy

[4]Center for Spintronic Materials, Amity University, UP Noida 201 313, India

pallavi.pandit@desy.de

agupta2@amity.edu

Abstract: A new strategy to nanoengineer gold/fluorocarbon multilayer (ML) nanostructures is reported. We have investigated the morphological changes occuring at the metal-polymer interface in multilayer structures with varying volume fraction of gold (Au) and the kinetic growth aspect of the microscale properties of nano-sized Au in plasma polymer fluorocarbon (PPFC). Investigations were carried out at various temperatures and annealing time by means of grazing incidence small-angle and wide-angle X-ray scattering (GISAXS and GIWAXS). We have fabricated a series of multilayers with variying volume fraction (0.12, 0.27, 0.38) of Au and bilayer periodicity in ML structure. They show an interesting granular structure consisting of nearly spherical shaped nanoparticles within the polymer layer. The nanoparticle (NP) morphology changes due to the collective effects of NPs diffusion within ensembles in the in-plane vicinity and inter-layer with increasing temperature. The in-plane NPs size distinctly increases (from 1.9 to 4 nm) with increasing temperature. The NPs become more spherical thus reducing the surface energy. Linear growth of NPs with temperature and time shows diffusion-controled growth of NPs in the ML structure. The structural stability of the multilayer is controlled by the volume ratio of the metal in polymer. At room temperature UV-Vis shows a blueshift of the plasmon peak from 560 nm in ML Au/PTFE_1 to 437 nm in Au/PTFE_3. We have identified the fabrication and post-deposition annealing conditions to limit the Local Surface Plasmon resonance (LSPR) shift (from $\Delta\lambda_{LSPR}$=180 nm (Au/PTFE_1) to $\Delta\lambda_{LSPR}$=67 nm (Au/PTFE_3 ML)) and their optical response over a wide visible wavelength range. A variation in the dielectric constant of the polymer in precence of varying Au inclusion is found to be the main factor affecting the LSPR frequency. Our finding may provide insights in Nano

Peer-reviewed version available at *Nanomaterials* **2019**, *9*, 1249; doi:10.3390/nano9091249

engineering ML structure can be useful to systematically control the growth of NPs in polymer matrix.

Keywords: *nanocomposite, metal-polymer-interface, multilayer, structure-function correlation, indirect band gap, GISAXS, GIWAXS, UV-Vis.*

Introduction: Easy processability, high flexibility and tunable physical properties, make nanocomposites very attractive for a broad range of applications. Recently, the combination of metal nanoparticles with dielectric media such as polymers has gained great pertinence both in fundamental as well as technological aspects. Their fine control and possible tuning of physical properties could lead to the fabrication of materials with novel functional, electric and optical properties and engender their accessibility to various applications in the field of optics, electronics and biomedicine[1–5]. These physical properties of the metal are strongly morphology dependent [6–9]. In particular, the metal undergoes a significant property change compared to the bulk due to the quantum confinement towards nanoscale and their large surface to volume ratio. Interfacial energy variation may also enhance their functionality [1]. Incorporation of metallic nanoparticles (NP) into a polymer improves the functionality of the polymer; govern by the metal-polymer interactions, which generally differ from the polymer−polymer interactions, the properties of the composite material are thus dominated by their interfacial interactions[10–13]. The morphologies of the embedded metal NPs can be artificially modified by controlling their processing parameters as preparation method, rate of deposition, thermal annealing etc. [6,9,10,14]. Besides this, the volume fraction of the metal in the polymer matrix plays a significant role in deciding the morphological structure. The conductivity of metal-polymer nanocomposites (MPNC) varies from insulating to conducting as a function of metal concentration. The resistivity drops by several orders of magnitude near percolation [15]. The conductivity depends exponentially on the cluster separation near the percolation threshold (insulator metal transition), which is proved by varying the metal-polymer volume fraction $\varphi = \frac{V_m}{V_p}$ with V_m & V_P being the volume of metal and polymer, respectively. Furthermore, in-plane growth of nanoparticles and their effect on the properties is limited by the percolation threshold as the metal layer above the percolation threshold gains a three-dimensional structure[1,6,16]. Varying the metallic volume fraction in the dielectric matrix also influences the refractive index and this can alter the optical properties of nanocomposite[17]. Additionally, thermal annealing of

Peer-reviewed version available at *Nanomaterials* **2019**, *9*, 1249; doi:10.3390/nano9091249

MPNC can also artificially modify the morphological structure due to enhancement of atomic mobility and diffusivity at higher temperature[18]. The resulting structure of NPs is then driven by nucleation, thermal mobility and growth. However, the fabrication and even more the control of the growth of nanoparticles for desired applications of such materials is still a major challenge. To study the individual particle growth, emphasis has been given to the MPNC multilayer (ML) structure of fixed volume fraction below the percolation threshold of metal in varying polymer layers. Such arrangement allows *inter alia* control growth of NPs in the polymer matrix. MPNC MLs have been prepared *via* sputter deposition having nanofabrication capability of sequential deposition of metal and polymer with the same precision[16,19]. Particularly, gold nanoparticles (Au NPs) modified plasma polymer fluorocarbon (PPFC)[20] (sputtered Polytetrafluorethylen (PTFE)) MLs has been prepared by alternating sputtering from an Au and a PTFE target. Au NPs in the PPFC matrix show long-term stability, brilliant optical properties and lead to a spectral optical shift upon variation in their size, shape and surrounding dielectric matrix[21]. PTFE has high chemical stability and comparatively high glass transition temperature with heat resistance capacity. It has low surface free energy that supports to grow spherical shape NPs, and a high sputter yield with low crosslinking tendency[22] making this polymer especially suitable for sputter deposition and for such studies. The correlation of the Au NPs morphology with the resulting optical properties of the MLs has been investigated in this study. The structural properties of the nanocomposites and kinetic growth of NPs in polymer matrix have been studied using grazing incidence small and wide angle X-ray scattering (GISAXS & GIWAXS). GISAXS yields the statistically pertinent horizontal and vertical correlation information of the changing electron density distribution [23,24] during growth, while GIWAXS can provide information about NPs crystallinity and kinetic growth of nanoparticles in polymer[25,26]. UV-Vis spectroscopy has been used to study the optical properties of nanocomposites[27,28]. The optical behavior of the nanocomposite evolves upon metal volume fraction variation due to the rearrangement of the NPs in the polymeric matrix. The range of the plasmon peak shift depends upon the density of implanted nanoparticles and the thickness of intermediate polymer layer. To contextualize further the structure-function correlations, we have performed isochronal thermal annealing of the ML structure and then compared the growth tendencies to the optical behavior. Hereby, the first question addressed is the effect of the metal volume fraction on the structural and optical properties of the nanocomposite.

The second one is the effect of temperature induced Au NPs growth behavior in PPFC matrix. Thus the relation of structural and optical properties during this growth is discussed.

Experimental Details:

Sample preparation: ML structure has been prepared on optically polished Si (100) substrate (Si-Mat, Germany). Prior to the deposition the Si wafers have been ultrasonically cleaned with acetone, iso-propanol and de-ionized water for 10 min. each followed by piranha cleaning. This strongly oxidizing chemical cleaning removes most organic matter and ion contamination from the substrate[29]. MPNC MLs were prepared by radio frequency (rf) ion beam sputtering, using alternating two independent gold (Mateck, Germany, purity 99.99%) and PTFE targets (Disk 2800 g/mol; Science Fellow Industries, India, purity 98%). Ion bombardment is initiated by a plasma glow discharge using a 3 cm broad-beam Kaufman-type hot-cathode at a low argon pressure (2.5 sccm), which thus generates Ar ions. The base pressure in the chamber was 3×10^{-7} mbar. The chamber was flushed with pure Ar (99.995%) a few times before deposition to minimize oxygen and water vapor contamination. The accelerating voltage and current were 1000 V and 30 mA, respectively. The target was kept at 45˚ with respect to the argon beam direction. The substrate was kept parallel to the target at a distance of 150 mm. The deposition pressure was 2.6×10^{-3} mbar. A schematic diagram for sputtering setup involved is shown in SI fig. S1. Three nanocomposites have been prepared by varying the Au volume fraction. The deposition rate of each of the materials (Au and PTFE) was determined separately at the same pressure and gas flow rate which was used for alternate sputtering. Deposited PTFE is named thereafter plasma polymer fluorocarbon (PPFC), due to their structural and chemical changes during sputtering. The effective thickness rates monitored were J_{Au}=0.92±0.03 Å/s and J_{PTFE} =3.4±0.2 Å/s. The filling factor of gold in three samples was 0.12, 0.27 and 0.38 which is below the gold percolation threshold of 0.45 as reported for gold in amorphous fluoroplastics[15]. The volume fraction was estimated by considering the film thickness ratio of Au and PTFE inside the ML structure. The thickness estimation for the various volume fractions has been detailed in the SI. The in-plane thickness of each gold layer was kept constant at 1.0±0.1 nm in the entire three MLs, whereas the thickness of the polymer layer varied in the three samples (as 19.0, 9.0 and 5.6 nm, respectively) to offer different volume fractions of

Peer-reviewed version available at Nanomaterials 2019, 9, 1249; doi:10.3390/nano9091249

Au in PPFC. The total thickness of the multilayer stack in all three cases was 140±5nm. The structures of the films were as follows: Si/SiO_2/ [Au(1nm)/PPFC(19nm)$]_7$; [Au(1nm)/PPFC(9nm)$]_{14}$ and [Au(1nm)/PPFC(5.6nm)$]_{21}$. The indices in subscript denote the total number of bi-layers in the three MLs. The samples named thereafter are Au/PPFC_1, Au/PPFC_2 and Au/PPFC_3.

Characterization: A monochromatic X-ray beam with a wavelength of 0.154 nm was used for the simultaneous GISAXS and GIWAXS measurements at the SAXS beamline (BL 5.2), Elettra synchrotron, Trieste[30]. The incident beam had a cross section of 1.2 mm (H) × 100 μm (V). The small angle scattering signal was recorded with a 2D image plate detector (MAR 300; pixel size of 150 × 150 μm^2). The image plate was kept in the forward direction at a distance of 1850±1 mm from the sample, to measure the scattered intensity in forward direction. The intensity of the incident and specular beam near q_y=0 nm^{-1} was attenuated with a partly transparent aluminum filter in the beam path. Measurements were performed at constant grazing incidence angle α_i ~ 0.45˚. For in-plane GIWAXS measurements, a Pilatus 100K (Dectris Ltd., Switzerland; pixel size of 172 × 172 μm^2) detector was kept at a distance of 327.7±0.5 mm in the film plane (tilted 55˚; sketch of detector position used for experiment is shown in SI fig. S2.) This detector distance had been fixed to cover the required angular range. The exposure time for each measurement was set to 300s for GISAXS and GIWAXS. To address possible effects of X-ray irradiation on the structure, the ML was initially exposed to the photon beam for a longer time: up to 20 min exposure, no significant change in the scattering pattern has been observed. Beyond a time of 20 min, a small broadening of the diffraction peaks and a decrease in peak intensities were observed. Accordingly, to avoid any effect of radiation damage during the measurements, after every scan the sample was shifted across the beam by 2 mm (sample size 20 × 20 mm^2) to expose a fresh area of the film. The angular detector ranges have been converted from pixel to the scattering vector q using as two standard samples calibration reference; rat tail tendon collagen for GISAXS and Cu foil for GIWAXS. The width of the calibrant Cu diffraction lines (W_{ins}) has been used as instrumental width for estimating the experimental crystalline size in the GIWAXS data of MLs using the Scherer formula[31]. The MLs were isochronally annealed at 373 K, 473K and 573 K *in-situ* during the measurement to study the kinetic growth of particles with time and temperature. A miniature boron nitride (BN) furnace (mounted on the

Preprints (www.preprints.org) | NOT PEER-REVIEWED | Posted: 27 June 2019 doi:10.20944/preprints201906.0287.v1

Peer-reviewed version available at *Nanomaterials* **2019**, *9*, 1249; doi:10.3390/nano9091249

sample rotation stage) was used for controlled heating of the sample, which was kept in a protective atmosphere of nitrogen gas. The sample temperature was maintained with an accuracy of ±0.5K. The optical reflectance spectra of the MPNCs were measured *ex-situ* with a UV-Vis spectrophotometer (Perkin Elmer, USA. Model: Lambda 950). The scans (normal incidence; reflectance mode) have been recorded in the wavelength range of 200nm to 800 nm. The main interest was to see the variation in surface plasmons of Au.

Results & discussion:

Structural properties at room temperature: An overview of the setup used for simultaneous GISAXS and GIWAXS measurements at the SAXS beamline (BL 5.2) Elettra, Trieste given in the supporting information (SI) fig. S3 (a).

GIWAXS: The 1D diffraction pattern (fig. S3 (b)) has been extracted from the 2D in-plane diffraction image of the sample in θ-2θ geometry. The GIWAXS pattern confirms the formation of well-established nanocrystalline particles due to the appearance of two diffraction peaks around $2\theta = 38.60\pm0.008^\circ$ and $43.30\pm0.003^\circ$, ascribed to the (111) and (200) planes of fcc crystalline Au. The peak positions are shifted to some extent from the bulk position which reflects the strain and which may be caused by the geometry and the polymer-filler interfacial interaction. Two Gaussians peak (red line in SI fig. S3 (b)) have been fitted to the data and the minimum crystalline size of a NP (D_{np}) has been derived from the width obtained for the (111) peak in the diffraction pattern, after deducting the instrumental width using the Scherer formula[31]:

$$D_{np} = \frac{0.94\lambda}{B\ \cos\theta}\ , B = \sqrt{W_E^2 - W_{ins}^2} \qquad (1)$$

where λ is the wavelength of the X-rays and B is the full width at half maximum in radians. W_E and W_{ins} (0.35 rad.) are the experimental and instrumental width, respectively. Results obtained are given in table 1. The lattice constant a nearly matches with the bulk value of Au (0.408 nm) which confirms crystalline gold nanoparticles in the polymer matrix. Diffraction plots of all three samples at room temperature are shown in the SI fig. S4 (d). As one can see from table 1, the crystalline size in all three MLs is almost the same despite of the varying volume fraction of gold in ML. This is as per expectation, since the deposited in-plane mass thickness of the individual gold layers is the same (1.0±0.1 nm) for all samples and

Peer-reviewed version available at *Nanomaterials* **2019**, *9*, 1249; doi:10.3390/nano9091249

the relative metal content is varied only by varying the thickness of the polymer layers.

Table 1: Au and polymer layer thicknesses, minimum crystalline size [111] (D), lattice constant (a), in-plane inter-particle distance (ξ_H) of all three multilayers at room temperature. Errors indicated only in the first line hold for all values.

Sample	δ(Au) (nm)	δ(PPFC) (nm)	D (nm)	a (nm)	ξ_H (nm)
Au/PPFC_1	1±0.1	19±0.8	2.43±0.004	0.403±0.001	4.30±0.05
Au/PPFC_2	1	9	2.46	0.404	4.34
Au/PPFC_3	1	5.6	2.45	0.406	4.32

GISAXS: In-plane cuts I(q_y) were made at the Yoneda peak of Si (q_z = 0.236 nm^{-1}) and the software package DPDAK[32] was used to extract quantitative information from the data sequence. Last Image taken at particular temperature is illustrated in fig. S5. Please note that a small tilt can be observed in the measured 2D pattern which we associate to an initial tilt in the heater assembly at which specimen was mounted (see SI fig. S3 for details of the setup). Tilt was accounted when making the cuts, see indicated area in fig. S5, first left column. The GISAXS pattern shows a broad side peak that emerges at large q_y values (fig. S3 (c)). This peak is related to a maximum interference of scattered waves describing the nanoparticle correlation distance, often called inter particle distance ξ_H[16,25,33]. From the position of the side peak (horizontal) one can estimate the average inter-particle (ξ_H) using the formula[16],

$$\xi_H \approx \frac{2\pi}{q_y} \qquad (2)$$

where, q_y is the position of the side peak in y direction. In the Yoneda cut I(q_y) at constant q_z = 0.236 nm^{-1} the presence of a peak (fig. S3(c)) evidences that the island distribution is not completely random, but are separated by a preferential nearest neighbor distance ξ (center-to-center), indicating short range ordering of Au NPs in PPFC. The side maxima observed for pristine MLs are dominated by the structure factor signals and indicate a substantial lateral ordering of the nanoparticles. The peak in the q_y range of 1.45−1.46 nm^{-1} corresponds to the inter particle distance $\xi_H \approx 4.3 \pm 0.05$ nm in real space, obtained by simulation (see SI for details). Yoneda cuts of three pristine samples are shown in the SI fig. S4 (e). The same inter-particle distances ξ_H

Preprints (www.preprints.org) | NOT PEER-REVIEWED | Posted: 27 June 2019 doi:10.20944/preprints201906.0287.v1

Peer-reviewed version available at *Nanomaterials* **2019**, *9*, 1249; doi:10.3390/nano9091249

were obtained for all three samples (see table 1), which corroborates a constant in-plane thickness of gold resulting in a uniform interlayer morphology. Similar to eq. 2, the vertical interlayer-particle distance ξ_V was derived using,

$$\xi_V \approx \frac{2\pi}{q_z} \qquad (3)$$

Where, q_z denotes the position of the first order Bragg peak in the off-detector cut.

The off-detector cut demonstrates the vertical ordering in MPNC, executed (along q_z) for $1.85\text{nm}^{-1} < q_y < 1.89\ \text{nm}^{-1}$ (fig. S3 (d)). In the vertical direction an estimable inter-particle correlation is observed due to the periodic structure of the MPNC ML. As the first Au layer is deposited on the Si wafer, Au NPs are formed which exhibit in-plane local ordering of a granular nanoclusters assembly[16,34]. The next deposited PPFC amorphous layer perfectly covers the Au NPs layer. The successive alternate deposition of Au and PPFC layers leads to the appearance of small undulations/ waviness with a period order given by the vertically interlayer-particle distance (ξ_V), see also fig. S4 (a). Layer-by-layer self-organized growth of NPs is the origin of this vertical order. The vertical order leads to well defined Bragg peaks in the scattering intensity from the MLs. The Bragg peaks in vertical direction show the strong structural coherence between the individual layers of the multilayers[35–37]. The off detector cuts of three MLs are given in S4 (f). The Bragg peak is shifted towards higher q values from sample Au/PPFC_1 to Au/PPFC_3. In these three films the polymer layer thickness has been intentionally reduced from Au/PPFC_1 to Au/PPFC_3 in order to obtain different volume fractions of gold in the total ML stack (fig. S4(a-c)). Thus the shift in the Bragg peak position signals the fact that the as the PPFC layer thickness decreases and hence the separation of the Bragg peaks increases (fig S4 (f)). The presence of a successive number of Bragg peaks in the GISAXS pattern of the MLs indicates that the NPs in the layers are well separated and the spacing between the Au NP layer is rather well established in Au/PPFC_1 as compared to Au/PPFC_2 and Au/PPFC_3. In addition, the peaks broaden from sample Au/PPFC_1 to Au/PPFC_3 (fig. S4 (f)). This can be understood such that the interfaces are not sharp, but rather show a diffuse compositional profile which is evidence of a strong intermixing of metal due to metal embedment in polymer at the interfaces in the pristine sample itself. This can be understood in terms of interface modulation[38] and stress in the three MLs according to the volume fraction of Au in PPFC. On the other hand Amarandei *et al.* reported that MPNCs the Au NPs interactions with the underlying layers must be

Peer-reviewed version available at Nanomaterials 2019, 9, 1249; doi:10.3390/nano9091249

considered[33,39]. For MLs Au/PPFC_2 and Au_PPFC3 the ratio of NP radius to polymer thickness is low enough that embedding interlayer interaction is thermodynamically favored[40]. The undulated structure of the PPFC films increases with decreasing PPFC layer thickness because of the thinner PPFC layer covers the waviness of the Au layers less efficient (see schematic structures shown in fig. S4 (a-c)). Consequently, the embedding of the Au inclusions in the intervening PPFC matrix increments, and the vertical coherence length decreases[37]. We further note that the intensity of the first Bragg peak (indicated by arrow in fig. S4 (f)) depends on the effective interdiffusivity/ embeding in the MLs.

Table 2: Interlayer-particle distance (ξ_V) calculated from the first order Bragg peak of the multilayers at various temperatures. The errors have given in one row hold for all three MLs with varying temperature. N.q.: not quantifiable.

Multilayer	ξ_V *(nm)* 273K	ξ_V *(nm)* 373K	ξ_V *(nm)* 473K	ξ_V *(nm)* 573K
Au/PPFC_1	10.45±0.03	9.79±0.04	9.18±0.07	5.13±0.1
Au/PPFC_2	6.86	6.61	4.65	n.q.
Au/PPFC_3	3.82	7.02	n.q.	n.q.

The interlayer-particle distance (ξ_V) is decreasing from ML Au/PPFC_1 to Au/PPFC_3, due to the decrease in the period in successive MLs (from 10.5 to 3.8 nm). This is in conformity with the constant in-plane gold thickness and varying polymer thickness in the three successive MLs. From the off detector cuts of pristine MLs (as given in fig. S4 (f)), the structure and morphology of the NPs in a vertical stack can be estimated. For extracting the lateral distance ξ_H, we performed a simulation of the GISAXS signal in the Yoneda cut using the software IsGISAXS [41]. Details are described in the SI (Fig. S6).

Structural Changes during and after Annealing:

GIWAXS: Annealing of the nanocomposite thin films well above the glass transition temperature (T_g) reduces the interaction bond strength between metal NPs and polymer molecules. The ML structure undergoes reorganization because of the change in the physical structure of the polymer at higher temperatures. The mobility of the NPs increases due to weaker interface interaction, being accompanied by a weaker

Peer-reviewed version available at *Nanomaterials* **2019**, *9*, 1249; doi:10.3390/nano9091249

entanglement density of the polymer chains. As a result, NPs start to diffuse through the polymer network. More and more NPs come in contact with each other, and eventually coagulation of these particles occurs[18,42]. This would increase the average crystalline/ nanoparticle size, inter-particle distance and may modify NPs morphology. As mentioned earlier, to study the effect of temperature on the nanocomposite properties isochronal thermal annealing of the MLs has been done at various temperatures. A number of scattering patterns has been recorded in period of 20 to 30 min. with exposure time of 298s each at intervals of 5 min. for statistical study. Thus, at each temperature a number of scattering pattern were recorded as a function of time. To estimate the kinetic behavior of the nanoparticles in the polymer matrix, the diffusion of NPs was estimated using the equation of diffusion[43,44],

$$D_{np}{}^2 = 2D_f t \qquad (4)$$

where D_{np} denotes the minimum crystalline size (Eq. 1), D_f is the diffusion constant and t is the annealing time. Figure 1(a) shows the variation of minimum crystalline size in Au/PPFC_3 as a function of $\sqrt{t}$ at different annealing temperatures. One can see that the crystalline size increases linearly as a function of $\sqrt{t}$ at all investigated temperatures, suggesting a diffusion-controlled growth of nanoparticles in the polymer matrix at the varying temperatures. The slope of the straight line is proportional to the diffusivity on NP's in polymer matrix. The variation in crystalline size was found to be systematic in all the samples (see SI figure S7 (a) & (b)). The obtained values of 'D_f' are used to find the activation energy (E_a) from the equation[37,45]

$$D_f = D_0 \exp\left(\frac{-E_a}{RT}\right) \qquad (4)$$

with R gas constant, D_0 pre-exponential factor and T the annealing temperature. From the slope of ln (D_f) and 1/T as shown in figure 1(b), the activation energy of Au NPs interdiffusion in Au/PPFC_3 results E_a = (0.34 ± 0.02 eV). Arrehenius-plots of ML Au/PPFC_1 and Au/PPFC_2 are given in SI fig. S7.

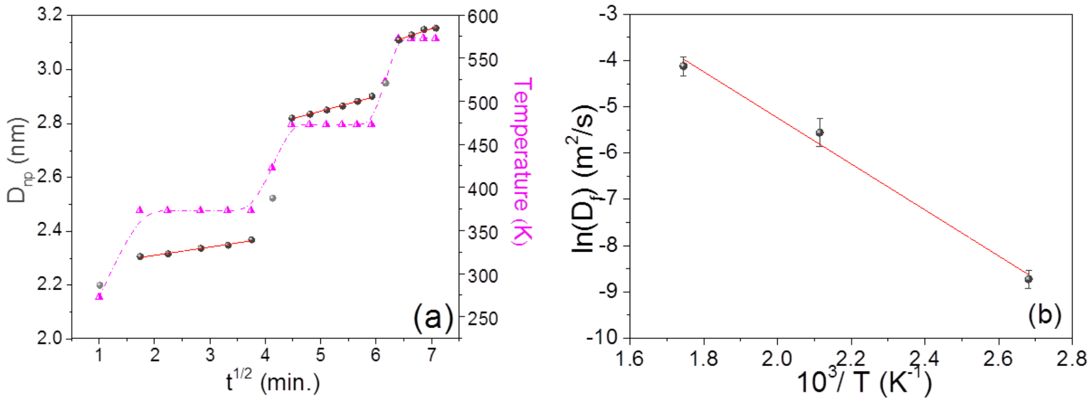

Figure 1: (a) Crystalline size (from GIWAXS) variation in Au/PPFC_3 as a function of annealing time $\left(\sqrt{t}\right)$ at varying temperature; the dotted (pink) curve represents the temperature profile of the sample with time and temperature (b) Arrhenius-plot showing the relationship between ln(D_f) (where, D_f is the diffusion constant) and 10^3/T for the Au/PPFC_3 ML obtained from in-situ temperature dependent in-plane GIWAXS.

The glass transition temperature of bulk PTFE is around 394 K. It is interesting to see from figure 1(b) that even at 373 K, which is below the glass transition temperature the diffusion of nanoparticles in polymer matrix is governed by the same activation energy as evidenced by the Arrhenius plot. A change in viscosity across the glass transition temperature is expected to result in a significant change in the diffusion mechanism of nanoparticles. The NP diffusion at all the three temperatures studied in the present work is governed by the same activation energy and suggests that no glass transition takes place in the temperature range investigated. The glass transition temperature is known to get reduced in the thin film form or with the inclusion of nanofillers[46,47]. Thus, it is quite likely that in the present system the glass transition temperature has gone below 373K (well above RT (273K) but less than 394K). The activation energy has been found decreasing from Au/PPFC_1 (1.03±0.02) eV to Au/PPFC_3 (0.340±0.02) eV [Au/PPFC_2 (0.429±0.02)]. This is due to the fact that the polymer intermediate barrier layer between two Au layers was successively decreased in the three MLs. Thus, the polymer layer mass density is in decreasing order, ensuring a decrease in activation energy.

GISAXS: The film morphology at various temperatures was accessed with GISAXS. 2D GISAXS pattern recorded at various temperatures are shown in figure S5. The Yoneda peak is accompanied by a broad side peak at higher q_y. Figures 2(a, b &c)

Peer-reviewed version available at *Nanomaterials* **2019**, *9*, 1249; doi:10.3390/nano9091249

gives Yoneda cuts made for the three MLs at different temperatures The lateral correlation peak in Au/PPFC_1 and Au/PPFC_2 is continuously shifting towards lower q_y up to 473 K and then slightly shifts to higher q_y at 573K signalizing first an increase in the inter particle distance of the NPs and then a slight decrease at 573K. In Au/PPFC_3 the inter-particle distance is continuously increasing with temperature up to 573K. In the ML structure, the diffusion of NPs at lower temperature is mostly confined within the Au layers, i.e. parallel to the substrate. But the NPs are gaining higher mobility both in horizontal and vertical direction with increasing temperature. At 573 K the polymer is close to its molten state and the NPs are thus gaining more freedom in both directions. The maximum in scattering intensity related to the NPs layer is fastly moving towards lower q_y at 573 K indicating a change in the particle distance ξ_H in the layer. Thus the inter-particle distance at higher temperature is due to the NPs mobility in both directions. However, Au/PPFC_3 has the lowest polymer layer thickness; due to this insufficient intermediate polymer thickness, it is not separating completely the Au NPs layers. Hence, the NPs are getting highest mobility already at lower temperature and the inter-particle distance is continuously increasing as a collective response of the mobility of NPs in both vertical and horizontal directions in the ML. It is worth mentioning that at higher temperature a higher order peak at larger q_y values (marked in fig. 2) occurs. This indicates a more ordered state of the structure due to the thermal annealing.

The in-plane average NPs radius R has been derived from the effective layer thickness (δ) of gold and inter-particle distance based on geometrical model by Schwartzkopf *et al.*[16] by applying it to spherical shaped NPs. The geometrical model assumes that the effective deposited material is locally separated into a hexagonal array of spherical shaped clusters in a distance ξ_H. According to this model assumption, the average radius of the supported clusters can be calculated by:

$$R = \sqrt[3]{\frac{3^{1.5}}{8\pi}\xi_H{}^2\delta} \qquad (6)$$

With effective thickness $\delta = 1.0\ \pm 0.1\ nm$ of Au and inter-particle distance ξ_H. Resulting sizes of the NPs for different temperatures are given in table 3.

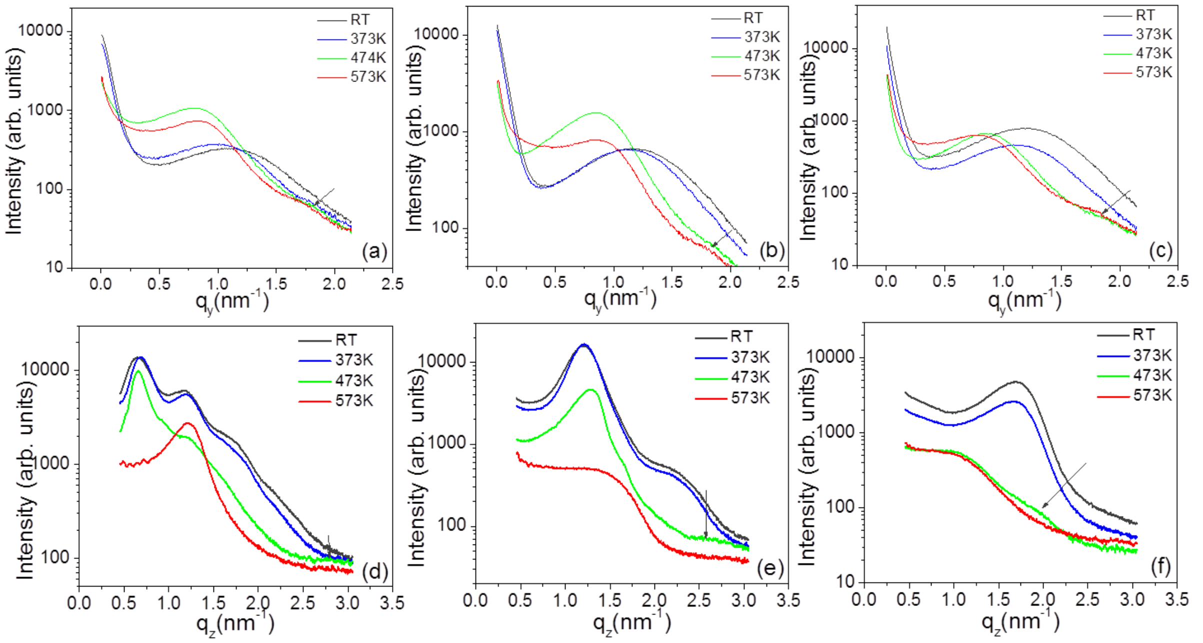

Figure 2: Cuts obtained from MLs various temperatures. Yoneda cuts are shown in (a, b, c) and off-detector cuts in (d, e, f) for MLs the MLs Au/PPFC_1, Au/PPFC_2 and Au/PPFC_3, respectively. In each plot, the arrow at higher q values denotes the presence of a higher order peak.

Particle radius has slightly decreased in MLs Au/PFC_1 and Au_PPFC_2 from temperature 473K to 573K. This might be to slight form change. Particle growth at various temperatures and their corresponding activation energy (0.109 ± 0.01eV) for interdiffusion of adjacent NPs through the polymer matrix is shown in fig. 3(a) & (b). One can observe a decrease in. activation energy from Au/PPFC_1 (0.572 ± 0.01eV) to Au/PPFC_2 (0.129 ± 0.01eV) given in fig S8. The activation energy is found to be lower in analysis of the particle growth study by GISAXS than by using the minimum crystalline size estimation *via* GIWAXS. The linear incremental trend in activation energy plot is same in both calculated from crystalline size (GIWAXS) and particle size (GISAXS). The results are consistent, as minimum crystalline size is less than the particle size and it is increasing with temperature.

Peer-reviewed version available at *Nanomaterials* **2019**, *9*, 1249; doi:10.3390/nano9091249

Table 3: NPs radius (R) and inter-particle distance (ξ_H) variation in three MLs with temperature. The values for the errors are given in line1 hold for all values in the columns.

Temperature	MLs	ξ_H (nm)	R (nm)
RT	Au/PPFC_1	4.30±0.05	1.56±0.003
	Au/PPFC_2	4.34	1.57
	Au/PPFC_3	4.32	1.57
373 K	Au/PPFC_1	5.20	1.67
	Au/PPFC_2	5.81	1.91
	Au/PPFC_3	5.92	1.93
473 K	Au/PPFC_1	6.92	2.02
	Au/PPFC_2	6.03	1.96
	Au/PPFC_3	6.31	2.01
573 K	Au/PPFC_1	6.48	1.94
	Au/PPFC_2	5.89	1.93
	Au/PPFC_3	6.35	2.03

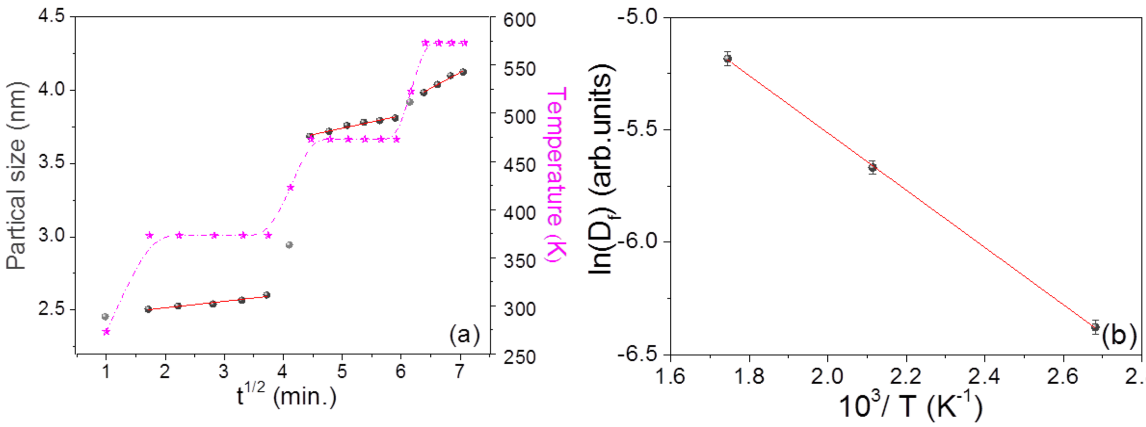

Figure 3: (a) Particle size variation in Au/PPFC_3 as a function of annealing time $(\sqrt{t})$ at varying temperature; the dotted (pink) curve represents the temperature profile of the sample with time and temperature (b) Arrhenius-plot showing the relationship between ln(D_f) and 10^3/T for the Au/PPFC_3 ML obtained from in-situ temperature dependent in-plane GISAXS; red line showing linear fit.

Off-detector cuts were also made from the data to analyze the changes occurring during annealing more carefully, they are shown in fig. 2(d,e & f). One can notice that at 373 K there is not a yet significant change in the Bragg peak position in all three

Peer-reviewed version available at Nanomaterials 2019, 9, 1249; doi:10.3390/nano9091249

MLs showing that the ordering is preserved below the glass transition temperature (T_g) (one should expect change in morphology crossing glass transition temperature), although there is small decrease in intensity that is due to the gradual mixing at the interfaces. However a further increase in temperature to 473 K results in a significant change in the structure. At 473 K the first Bragg peak in Au/PPFC_1 ML is slightly shifted towards lower q_z while for other two MLs the Bragg peak is shifting towards higher q_z and the higher order Bragg peaks become suppressed. This might be because of a rearrangement of the NPs in PPFC leading to a more compact structure of the ML with higher intermixing at the metal-polymer interface. A further increase in temperature results in a rapid decrease in interlayer particle distance (ξ_V). Although ξ_V is decreased remarkably at 573K the presence of a broad Bragg peak or hump shows that the layered structure is still sustained. The Bragg peak is increasingly broadening from ML Au/PPFC_1 to Au/PPFC_3 as a result of higher intermixing at elevated temperature. This transformation shows that the MLs are converted into a diffused metal-polymer structure at 573K. The interlayer particle distance of the MLs at various temperatures is listed in table 2.

Optical properties at room temperature: Ordered nanoparticles are promising structures that enable interconversion of the propagation of electromagnetic waves and thus thereby promote strongly enhanced local fields used for a number of practical applications like photonics, optical sensors etc[42,48,49]. UV-Vis spectra of the three pristine multilayers are shown in fig. 4. The spectra have been taken in off-specular reflection mode; dips in the spectra are due to absorption. One can notice characteristic features associated with NP assembly and their arrangement in the ML structure. In the wavelength range of 250 nm to 400 nm some interference effect is seen[50] because of the multilayer structure. In the higher wavelength region a surface plasmon is emerging in the spectrum, indicated by the diamond symbols in fig. 4. UV-Vis spectra of nanocomposites are showing strong absorption in the range of 440 nm to around 520 nm. In present case we will refer this as local surface plasmon (LSPR) as in ML structure NPs layer are buried in polymer matrix. One can notice the presence of a single plasmon in ML Au/PPFC_1 while for Au/PPFC_2 and Au/PPFC_3 the plasmon splits in two.

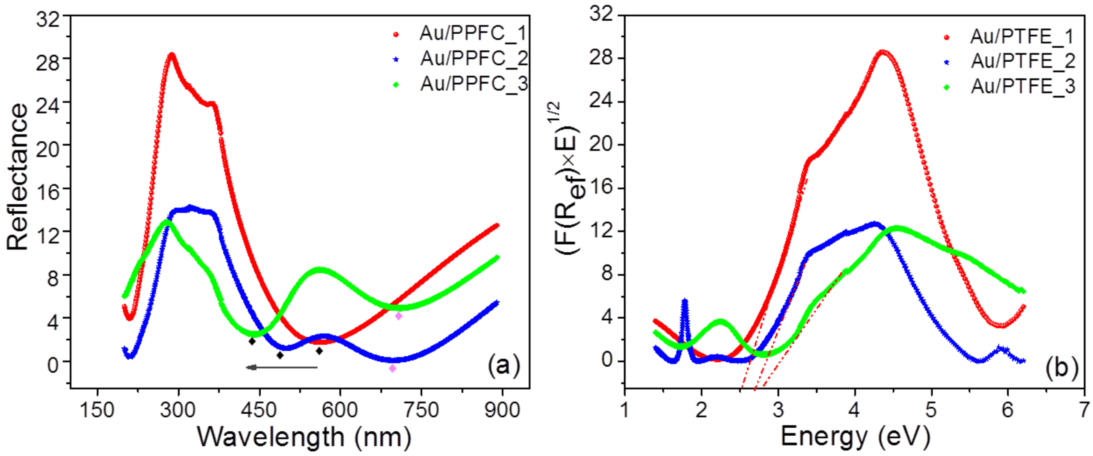

Figure 4: (a) UV-Vis spectra of Au/PPFC MPNCs room temperature; the local surface plasmon resonance (LSPR) in the three MLs are indicated by a diamond symbol (♦) and the arrow indicates the shift in LSPR (b) Plot of [$F\left(R_{ef}\right) \times (h\nu)$] vs. Energy for indirect band gap calculation by applying linear approximations (fits are indicated by the red dash-dotted lines).

A single broad Gaussian plasmon dip in the reflection spectra can be indication for a spherical shape of the NPs[51,52]. The analysis has been done considering the spherical shape of the nanoparticles, which was also confirmed by the GISAXS data. The optical study shows that the electric field distribution across the surface of the spherical particle seems to be uniform, and thus all the free conduction electrons oscillate in-phase, resulting in one plasmon, regardless of the type of incident polarization[53,54]. The isotropic optical response of the spherical particles can be altered either by increasing their aspect ratio (changing the particles morphology) or coupling, i.e. placing them in close proximity of other particles[49,55–57]. In Au/PPFC_1 the periodic polymer thickness is 19 nm which ensures that the voids between NPs become completely filled with PPFC. The structurally continuous polymer barrier layer completely separates the metallic layer vertically, which in turn hinders the effective movement of nanoparticles in vertical direction (fig. S4 (a)). Thus an ultra-fine constant thickness of 1 nm of gold ensures local monodispersion of in-plane particles with small size variation which supports the appearance of a single plasmon in Au/PPFC_1. Local monodisperse distribution of NPs has also been confirmed by GISAXS. In the other 2 MLs. because of the lower thicknesses of polymer (9 nm and 5.6 nm, respectively), the polymer film is not continuous, but PPFC grows preferentially within the voids between neighboring particles. The over layer PPFC

Peer-reviewed version available at Nanomaterials 2019, 9, 1249; doi:10.3390/nano9091249

thickness is not capable to isolate metal NPs completely in a vertical stack. As a consequence, the NPs distance becomes small enough to give rise to plasmon coupling between the interacting particles, which changes the distribution of the induced surface dipoles and hence the electric field (fig. S4 (b & c)). This yields a disturbance in the electronic oscillations which can result in a change in the optical response and thus lead to the excitation of more than one plasmon mode (PM)[55–57]. The broadening of plasmon indicates a broad distribution of particle sizes in the MLs. The reflection amplitude increases with the metal filling factor, which shows that the NP density is directly proportional to the absorption intensity[58]. Sequels to this plasmon are shifted to lower wavelength (blue shift) from sample Au/PPFC_1 to Au/PPFC_3. There are a number of reasons that can lead to the observed blue plasmon shift. The optical properties of nanocomposites are highly sensitive to the morphology and the surrounding dielectric medium. The decrease in particle size or increase in inter-particle distance can result in a blue shift of the plasmon[3,59,60]. In the present case, the Au NP size and inter-particle distance in the three pristine samples have been found to be almost the same (confirmed by GISAXS & GIWAXS), so we may exclude this reason for the blue shift of the plasmon in our system. Amongst the possible causes for this effect, the only possible reason for the observed blue shift in the present case should be related to a possible variation in the refractive index of the polymer in the vicinity of the metal particles[7,48]. As in the present study we have varied the polymer thickness in the multilayers, this may induce that the mass density of the polymer has been varied. Due to this, the polymer-filler bonding would vary; this structural change can alter the refractive index of the polymer[61,62]. From the perspective of this information we think that this could be the possible reason of the plasmon blue shift in the present case. LSPR of gold nanoparticles can be used to assess the information on the binding energy. To quantify this, the indirect band gape energy of the three MLs has been calculated using the Kubelka–Munck radiative transfer model[63–65].

$$F(hv) = \left(F\left(R_{ef}\right) \times E\right)^{1/2},\ F\left(R_{ef}\right) = \frac{(1-R_{ef})^2}{2R_{ef}} \qquad (7)$$

with R_{ef} is the reflectance. The model allows the calculation of the reflectance from a layer that both scatters and absorbs light. The linear fit through the LSPR yield the indirect band gap energy of the system. Figure 4(b) depicts the plot of $\left(F\left(R_{ef}\right) \times E\right)^{1/2}$ vs energy for three MLs at room temperature and indicates the linear fit applied.

doi:10.20944/preprints201906.0287.v1

Peer-reviewed version available at *Nanomaterials* **2019**, *9*, 1249; doi:10.3390/nano9091249

Resulting extrapolated values are given in table 4. One can see that, as one goes from sample Au/PPFC_1 to Au/PPFC_3, the indirect band gap exhibits a systematic increase. According to the Penn model[66] for the dielectric constant of semiconductor materials[67,68] and other materials[69] varies inversely with the band gap energy. Thus as one goes from Au/PPFC_1 to Au/PPFC_3 the dielectric constant is expected to decrease which should results in blue shift of SPR, as observed in the present case and corroborates our hypothesis. These findings elucidate the nature of plasmon modes in this ML system, which involves strong light-matter coupling, and set the level for the controlled bond formation by light excitation.

Table 4: Evaluated indirect band gap energy (in eV) for three multilayers at different temperature. The uncertainty is mentioned in line 1 only holds for all values in the column.

Sample	RT	373 K	473 K	573 K
Au/PPFC_1	2.51±0.04	2.61±0.03	2.67±0.05	3.18±0.03
Au/PPFC_2	2.58	2.82	2.94	3.70
Au/PPFC_3	2.66	2.85	2.93	2.95

Temperature dependent optical response: The sensitivity of the nanocomposite film to the host medium was tested by monitoring the change in the Au-LSPR position as a function of temperature. The multilayers were *ex-situ* annealed at 373K, 473K and 573K with same annealing protocol used for GISAXS and GIWAXS measurements and their UV-Vis spectra have been recorded. From figure S9, one can see that in all the three cases the LSPR peak exhibits a blue shift with increasing annealing temperature. Further, the magnitude of the shift decreases as one goes from sample Au/PPFC_1 to Au/PPFC_3 (fig. S10). Even a slight change from non-spherical to spherical shape can lead to a blue shift of the plasmon[70,71]. The band width of the LSPR band of the annealed sample indicates only a small variation in the size distribution. In general, by annealing the samples well above T_g of the polymer, the response to the dielectric environment significantly enhanced. The increased sensitivity of the annealed sample is attributed to the increased mobility of both polymer chains and gold nanoparticles in the close molten state of the polymer. As discussed earlier, the polymer layer thickness between two gold layers has been intentionally varied for the tuning of the structural and optical properties. Due to that with decreasing polymer layer thickness the embedding of the gold nanoparticles has changed from sparse to a denser form. The NPs size getting higher with thermal annealing and more massive particles move slowly and this is why the magnitude of the shift is decreased from Au/PPFC_1 to Au/PPFC_3 (fig. S10). The results obtained are summarized in table 4. The results show that, by using adequate post deposition annealing, a tailoring of the optical properties of such Au/PPFC MPNC MLs is possible and could be preferential for plasmonic-driven applications. From table 4 one can see an increase in the band gap energy with increasing temperature. This shows a higher mismatch of the crystal momentum in valence and conduction band[72]. Qualitatively, according to the Penn model, this is particularly showing the decrement of the dielectric constant (refractive index). An increase of the dielectric constant would lead to a shift of the absorption maximum towards longer wavelengths[73,74]. However, the present results are in conformity with a decreasing dielectric constant, as the dielectric constant is supposed to decrease from Au/PPFC_1 to Au/PPFC_3, which leads to a blue shift of Plasmon.

Conclusion: As promising Nano engineered ML structure, considered as a simple and practical system, enables us to control optical response that can be highly tuned. A well-defined interlayer inter-particle correlation is observed in all the three pristine MLs with an average in-plane inter-particle distance of about 4.30±0.05 nm in conformity with simulations. Furthermore, a strong inter-particle correlation is observed in vertical direction as well, in corroboration of the bilayer period variation in the three MLs. With thermal annealing the reordering of nanoparticles occurs and morphological changes were observed. The dependence of the nanoparticles size on the square root of the annealing time suggests a diffusion controlled growth of nanoparticles. These findings indicate that the mobility of metal nanoparticles can be affected by the volume fraction of metal in a polymer, and annealing significantly influences the NPs growth and ordering in a layered structure. An enhanced diffusion and intermixing is the main reason for the structure changes. It is worth noting that after annealing at 573K the inter particle correlation became more isotropic in both in-plane/ horizontal and vertical directions. At the same time NP size increases with increasing temperature and they become more spherical due to a reduction in the surface energy. The fraction of embedded NPs can be controlled by the annealing time and temperature. Thus, overall control of the metal volume fraction can be obtained. The stability limit can be shifted

Peer-reviewed version available at *Nanomaterials* **2019**, *9*, 1249; doi:10.3390/nano9091249

to higher temperature by varying the intermediate polymer layer thickness, which can be useful in device applications. UV-Vis analysis shows that the LSPR frequency exhibits a systematic variation with the volume fraction as well as with thermal annealing. The variation in the dielectric constant of the material is found to be the main factor affecting the LSPR frequency. The structural properties of the MLs are found in good agreement with their optical response. This work opens the way to tune the optical properties *via* controlling the growth of metal NPs. By virtue of our current approach one can systematically control the structural and optical properties of nanocomposite systems.

References:

1. Faupel, F.; Zaporojtchenko, V.; Strunskus, T.; Elbahri, M. Faupel. *Advanced Engineering Materials* **2010**, *12*, 1177–1190.
2. Sanchez, C.; Belleville, P.; Popall, M.; Nicole, L. Applications of advanced hybrid organic–inorganic nanomaterials: from laboratory to market. *Chemical Society Reviews* **2011**, *40*, 696–753.
3. Srivastava, S.; Haridas, M.; Basu, J.K. Optical properties of polymer nanocomposites. *Bulletin of Materials Science* **2008**, *31*, 213–217.
4. Lopes, W.A.; Jaeger, H.M. Hierarchical self-assembly of metal nanostrucures on diblock copolymer scaffolds. *Nature* **2001**, *414*, 735–738.
5. Turković, A.; Dubček, P.; Juraić, K.; Drašner, A.; Bernstorff, S. SAXS Studies of tio2 Nanoparticles in Polymer Electrolytes and in Nanostructured Films. *Materials* **2010**, *3*, 4979–4993.
6. Schwartzkopf, M.; Santoro, G.; Brett, C.J.; Rothkirch, A.; Polonskyi, O.; Hinz, A.; Metwalli, E.; Yao, Y.; Strunskus, T.; Faupel, F.; et al. Real-Time Monitoring of Morphology and Optical Properties during Sputter Deposition for Tailoring Metal-Polymer Interfaces. *ACS Applied Materials and Interfaces* **2015**, *7*, 13547–13556.
7. Alsawafta, M.; Badilescu, S.; Paneri, A.; Truong, V. Van; Packirisamy, M. Gold-poly(methyl methacrylate) nanocomposite films for plasmonic biosensing applications. *Polymers* **2011**, *3*, 1833–1848.
8. Roth, S. V.; Santoro, G.; Risch, J.F.H.; Yu, S.; Schwartzkopf, M.; Boese, T.; Döhrmann, R.; Zhang, P.; Besner, B.; Bremer, P.; et al. Patterned Diblock Co-Polymer Thin Films as Templates for Advanced Anisotropic Metal Nanostructures. *ACS Applied Materials and Interfaces* **2015**, *7*, 12470–12477.

9. Hua, Y.; Chandra, K.; Dam, D.H.M.; Wiederrecht, G.P.; Odom, T.W. Shape-Dependent Nonlinear Optical Properties of Anisotropic Gold Nanoparticles. *The Journal of Physical Chemistry Letters* **2015**, *6*, 4904–4908.
10. Torrisi, V.; Ruffino, F. Metal-Polymer Nanocomposites: (Co-Evaporation/(Co)Sputtering Approaches and Electrical Properties. *Coatings* **2015**, *5*, 378–424.
11. Ciprari, D.; Jacob, K.; Tannenbaum, R. Characterization of Polymer Nanocomposite Interphase and Its Impact on Mechanical Properties. *Macromolecules* **2006**, *39*, 6565–6573.
12. Li, S.; Meng Lin, M.; Toprak, M.S.; Kim, D.K.; Muhammed, M. Nanocomposites of polymer and inorganic nanoparticles for optical and magnetic applications. *Nano Reviews* **2010**, *1*, 5214.
13. Shen, Y.; Lin, Y.; Nan, C.W. Interfacial effect on dielectric properties of polymer nanocomposites filled with core/shell-structured particles. *Advanced Functional Materials* **2007**, *17*, 2405–2410.
14. Guozhong C *Nanostructures & Nanomaterials: Synthesis, Properties & Applications*; 2nd, Ed.; Imperial College Press: London, UK, 2004; ISBN 1-86094-4159.
15. Takele, H.; Schürmann, U.; Greve, H.; Paretkar, D.; Zaporojtchenko, V.; Faupel, F. Controlled growth of Au nanoparticles in co-evaporated metal/polymer composite films and their optical and electrical properties. *The European Physical Journal Applied Physics* **2006**, *33*, 83–89.
16. Schwartzkopf, M.; Buffet, A.; Körstgens, V.; Metwalli, E.; Schlage, K.; Benecke, G.; Perlich, J.; Rawolle, M.; Rothkirch, A.; Heidmann, B.; et al. From atoms to layers: in situ gold cluster growth kinetics during sputter deposition. *Nanoscale* **2013**, *5*, 5053.
17. Kelly, K.L.; Coronado, E.; Zhao, L.L.; Schatz, G.C. The Optical Properties of Metal Nanoparticles: The Influence of Size, Shape, and Dielectric Environment. *The Journal of Physical Chemistry B* **2003**, *107*, 668–677.
18. Heilmann A *Polymer Films with Embedded Metal Nanoparticles*; Springer: Berlin, Germany, 2003; ISBN 978-3540431510.
19. Zaporojtchenko, V.; Podschun, R.; Schürmann, U.; Kulkarni, A.; Faupel, F. Physico-chemical and antimicrobial properties of co-sputtered Ag-Au/PTFE nanocomposite coatings. *Nanotechnology* **2006**, *17*, 4904–4908.

Peer-reviewed version available at *Nanomaterials* **2019**, *9*, 1249; doi:10.3390/nano9091249

20. Kim, S.H.; Kim, M.; Lee, J.H.; Lee, S.-J. Self-Cleaning Transparent Heat Mirror with a Plasma Polymer Fluorocarbon Thin Film Fabricated by a Continuous Roll-to-Roll Sputtering Process. *ACS Applied Materials & Interfaces* **2018**, *10*, 10454–10460.
21. Lahav, M.; Vaskevich, A.; Rubinstein, I. Biological sensing using transmission surface plasmon resonance spectroscopy. *Langmuir* **2004**, *20*, 7365–7367.
22. Zekonyte, J.; Zaporojtchenko, V.; Faupel, F. Investigation of the drastic change in the sputter rate of polymers at low ion fluence. *Nuclear Instruments and Methods in Physics Research B* **2005**, *236*, 241–248.
23. Schwartzkopf, M.; Roth, S. Investigating Polymer–Metal Interfaces by Grazing Incidence Small-Angle X-Ray Scattering from Gradients to Real-Time Studies. *Nanomaterials* **2016**, *6*, 239.
24. Kaune, G.; Ruderer, M.A.; Metwalli, E.; Wang, W.; Couet, S.; Schlage, K.; Röhlsberger, R.; Roth, S. V.; Müller-Buschbaum, P. In Situ GISAXS Study of Gold Film Growth on Conducting Polymer Films. *ACS Applied Materials & Interfaces* **2009**, *1*, 353–360.
25. Müller-Buschbaum, P. Applications of Synchrotron Light to Scattering and Diffraction in Materials and Life Sciences: A Basic Introduction to Grazing Incidence Small-Angle X-Ray Scattering. *Lect. Notes in Phys.* **2009**, *776*, 61–89.
26. Hexemer, A.; Müller-Buschbaum, P. Advanced grazing-incidence techniques for modern soft-matter materials analysis. *IUCrJ* **2015**, *2*, 106–125.
27. Choi, J.; Choi, M.-J.; Yoo, J.-K.; Park, W.I.; Lee, J.H.; Lee, J.Y.; Jung, Y.S. Localized surface plasmon-enhanced nanosensor platform using dual-responsive polymer nanocomposites. *Nanoscale* **2013**, *5*, 7403.
28. Novotny, L.; Hecht, B. Surface plasmon -. In *Principles of Nano-Optics*; Cambridge University Press., 2012; pp. 407–450 ISBN 9780511813535.
29. Pandit, P.; Banerjee, M.; Pandey, K.K.; Sharma, S.M.; Gupta, A. Role of substrate in melting behavior of Langmuir-Blodgett films. *Colloids and Surfaces A: Physicochemical and Engineering Aspects* **2015**, *471*, 159–163.
30. Amenitsch, H.; Bernstorff, S.; Kriechbaum, M.; Lombardo, D.; Mio, H.; Rappolt, M.; Laggner, P. Performance and First Results of the ELETTRA High-Flux Beamline for Small-Angle X-ray Scattering. *Journal of Applied Crystallography* **1997**, *30*, 872–876.

31. Bushroa, A.R.; Rahbari, R.G.; Masjuki, H.H.; Muhamad, M.R. Approximation of crystallite size and microstrain via XRD line broadening analysis in TiSiN thin films. *Vacuum* **2012**, *86*, 1107–1112.
32. Benecke, G.; Wagermaier, W.; Li, C.; Schwartzkopf, M.; Flucke, G.; Hoerth, R.; Zizak, I.; Burghammer, M.; Metwalli, E.; Müller-Buschbaum, P.; et al. A customizable software for fast reduction and analysis of large X-ray scattering data sets: Applications of the new DPDAK package to small-angle X-ray scattering and grazing-incidence small-angle X-ray scattering. *Journal of Applied Crystallography* **2014**, *47*, 1797–1803.
33. Levine, J.R.; Cohen, J.B.; Chung, Y.W. Thin film island growth kinetics: a grazing incidence small angle X-ray scattering study of gold on glass. *Surface Science* **1991**, *248*, 215–224.
34. Babonneau, D.; Petroff, F.; Maurice, J.L.; Fettar, F.; Vaurès, A.; Naudon, A. Evidence for a self-organized growth in granular Co/Al2O3multilayers. *Applied Physics Letters* **2000**, *76*, 2892–2894.
35. Fullerton, E.E.; Schuller, I.K.; Vanderstraeten, H.; Bruynseraede, Y. Structural refinement of superlattices from x-ray diffraction. *Physical Review B* **1992**, *45*, 9292–9310.
36. Fullerton Eric E.; Kumar S; Grimsditch M.; Kelly David M; Schuller Ivan K X-ray-diffraction characterization and sound-velocity measurements of W/Ni multilayers. *Physsical Review B* **1993**, *48*, 2560–2567.
37. Reddy Raghavendra, V.; Gupta, A.; Gome, A.; Leitenberger, W.; Pietsch, U. In situ x-ray reflectivity and grazing incidence x-ray diffraction study of L 10 ordering in 57Fe/Pt multilayers. *Journal of Physics Condensed Matter* **2009**, *21*.
38. Shia D; Hui C. Y.; Burnside S. D.; Giannelis E. P. An Interface Model for the Prediction of Young ' s Modulus of Layered S i l icate-Elast om er Na nocom posi tes. *Polymer Composites* **1998**, *19*, 608–617.
39. Amarandei, G.; O'Dwyer, C.; Arshak, A.; Corcoran, D. The stability of thin polymer films as controlled by changes in uniformly sputtered gold. *Soft Matter* **2013**, *9*, 2695.
40. Amarandei, G.; Clancy, I.; O'Dwyer, C.; Arshak, A.; Corcoran, D. Stability of Ultrathin Nanocomposite Polymer Films Controlled by the Embedding of Gold Nanoparticles. *ACS Applied Materials & Interfaces* **2014**, *6*, 20758–20767.

Peer-reviewed version available at *Nanomaterials* **2019**, *9*, 1249; doi:10.3390/nano9091249

41. Lazzari, R. IsGISAXS: A program for grazing-incidence small-angle X-ray scattering analysis of supported islands. *Journal of Applied Crystallography* **2002**, *35*, 406–421.
42. Etrich, C.; Fahr, S.; Hedayati, M.; Faupel, F.; Elbahri, M.; Rockstuhl, C. Effective Optical Properties of Plasmonic Nanocomposites. *Materials* **2014**, *7*, 727–741.
43. Pradell, T.; Crespo D; Clavaguera N; Clavaguer-Mora M T. Diffusion controlled grain growth in primary crystallization : Avrami exponents revisited Diffusion controlled grain growth in primary crystallization : Avrami exponents revisited. *Journal of Physics: Condensed Matter* **1998**, *10*, 3833–3844.
44. Gupt, P.; Gupta, A.; Shukl, A.; Ganguli, T.; Sinha, A.K.; Principi, G.; Maddalena, A. Structural evolution and the kinetics of Cu clustering in the amorphous phase of Fe-Cu-Nb-Si-B alloy. *Journal of Applied Physics* **2011**, *110*.
45. Gupta, A.; Gupta, M.; Chakravarty, S.; Wille, H.; Leupold, O. Fe diffusion in amorphous and nanocrystalline alloys studied using nuclear resonance reflectivity. *Physical Review B* **2005**, *72*, 1–8.
46. Bansal, A.; Yang, H.; Li, C.; Cho, K.; Benicewicz, B.C.; Kumar, S.K.; Schadler, L.S. Quantitative equivalence between polymer nanocomposites and thin polymer films. *Nature Materials* **2005**, *4*, 693–698.
47. Forrest, J.A.; Mattsson, J. Reductions of the glass transition temperature in thin polymer films: Probing the length scale of cooperative dynamics. *Physical Review E* **2000**, *61*, 53–56.
48. Garcia, M.A. Surface plasmons in metallic nanoparticles: fundamentals and applications. *Journal of Physics D: Applied Physics* **2011**, *44*, 283001.
49. Reinhard, B.M.; Siu, M.; Agarwal, H.; Alivisatos, A.P.; Liphardt, J. Calibration of Dynamic Molecular Rulers Based on Plasmon Coupling between Gold Nanoparticles. *Nano Letters* **2005**, *5*, 2246–2252.
50. Kats, M.A.; Capasso, F. Optical absorbers based on strong interference in ultra-thin films. *Laser and Photonics Reviews* **2016**, *10*, 735–749.
51. Felidj, N.; Auberd, J.; Levi, G. Discrete Dipole Approximation for Ultraviolet-Visible Extiction Spectra Simulation of Silver and Gold Colloids. *J. Chem. Phys* **1999**, *111*, 1195–1208.
52. Mulfinger, L.; Solomon, S.D.; Bahadory, M.; Jeyarajasingam, A. V; Rutkowsky,

Peer-reviewed version available at *Nanomaterials* **2019**, *9*, 1249; doi:10.3390/nano9091249

S.A.; Boritz, C. Synthesis and study of silver nanoparticles. *Journal of chemical education* **2007**, *84*, 322.

53. Jensen, T.R.; Schatz, G.C.; Van Duyne, R.P. Nanosphere Lithography: Surface Plasmon Resonance Spectrum of a Periodic Array of Silver Nanoparticles by Ultraviolet−Visible Extinction Spectroscopy and Electrodynamic Modeling. *The Journal of Physical Chemistry B* **1999**, *103*, 2394–2401.
54. Hulteen, J.C.; Van Duyne, R.P. Nanosphere lithography: A materials general fabrication process for periodic particle array surfaces. *Journal of Vacuum Science & Technology A: Vacuum, Surfaces, and Films* **1995**, *13*, 1553–1558.
55. Voshchinnikov, N. V.; Farafonov, V.G. Optical properties of spheroidal particles. *Astrophysics and Space Science* **1993**, *204*, 19–86.
56. Chu, Y.; Banaee, M.G.; Crozier, K.B. Double-resonance plasmon substrates for surface-enhanced raman scattering with enhancement at excitation and stokes frequencies. *ACS Nano* **2010**, *4*, 2804–2810.
57. Zhou, Y.; Li, X.; Ren, X.; Yang, L.; Liu, J. Designing and fabricating double resonance substrate with metallic nanoparticles–metallic grating coupling system for highly intensified surface-enhanced Raman spectroscopy. *The Analyst* **2014**, *139*, 4799–4805.
58. Hedayati, M.K.; Fahr, S.; Etrich, C.; Faupel, F.; Rockstuhl, C.; Elbahri, M. The hybrid concept for realization of an ultra-thin plasmonic metamaterial antireflection coating and plasmonic rainbow. *Nanoscale* **2014**, *6*, 6037–6045.
59. El-Brolossy, T.A.; Abdallah, T.; Mohamed, M.B.; Abdallah, S.; Easawi, K.; Negm, S.; Talaat, H. Shape and size dependence of the surface plasmon resonance of gold nanoparticles studied by Photoacoustic technique. *The European Physical Journal Special Topics* **2008**, *153*, 361–364.
60. Ahmad, T.; Wani, I.A.; Ahmed, J.; Al-Hartomy, O.A. Effect of gold ion concentration on size and properties of gold nanoparticles in TritonX-100 based inverse microemulsions. *Applied Nanoscience* **2014**, *4*, 491–498.
61. Ghanipour, M.; Dorranian, D. Effect of Ag-Nanoparticles Doped in Polyvinyl Alcohol on the Structural and Optical Properties of PVA Films. *Journal of Nanomaterials* **2013**, *2013*, 1–10.
62. Scaffardi, L.B.; Tocho, J.O. Size dependence of refractive index of gold nanoparticles. *Nanotechnology* **2006**, *17*, 1309–1315.
63. Hecht, H.G. The Interpretation of Diffuse Reflectance Spectra. *J. Res. NBS A*

Peer-reviewed version available at *Nanomaterials* **2019**, *9*, 1249; doi:10.3390/nano9091249

Phys. Ch. **1976**, *80*, 567–583.

64. MURPHY, A. Band-gap determination from diffuse reflectance measurements of semiconductor films, and application to photoelectrochemical water-splitting. *Solar Energy Materials and Solar Cells* **2007**, *91*, 1326–1337.
65. R, L.; R, G. Band-gap energy estimation from diffuse reflectance measurements on sol–gel and commercial TiO2: a comparative study. *Journal of Sol-Gel Science and Technology* **2012**, *61*, 1–7.
66. Penn, D.R. Wave-number-dependent dielectric function of semiconductors. *Physical Review* **1962**, *128*, 2093–2097.
67. Ravindra, N.M.; Ganapathy, P.; Choi, J. Energy gap-refractive index relations in semiconductors - An overview. *Infrared Physics and Technology* **2007**, *50*, 21–29.
68. Aziz, S.B.; Rasheed, M.A.; Ahmed, H.M. Synthesis of polymer nanocomposites based on [methyl cellulose]<inf>(1-x)</inf>:(CuS)<inf>x</inf> (0.02M ≤ x ≤ 0.08 M) with desired optical band gaps. *Polymers* **2017**, *9*, 194.
69. Gupta K., S.; Singh, J.; Akhtar, J. Materials and Processing for Gate Dielectrics on Silicon Carbide (SiC) Surface. In *Physics and Technology of Silicon Carbide Devices*; 2013; pp. 207–234 ISBN 978-953-51-0917-4.
70. Portalès, H.; Pinna, N.; Pileni, M.P. Optical response of ultrafine spherical silver nanoparticles arranged in hexagonal planar arrays studied by the DDA method. *Journal of Physical Chemistry A* **2009**, *113*, 4094–4099.
71. Pileni, M.P. Optical properties of nanosized particles dispersed in colloidal solutions or arranged in 2D or 3D superlattices. *New Journal of Chemistry* **1998**, *22*, 693–702.
72. Trainer, D.J.; Putilov, A. V.; Di Giorgio, C.; Saari, T.; Wang, B.; Wolak, M.; Chandrasena, R.U.; Lane, C.; Chang, T.R.; Jeng, H.T.; et al. Inter-Layer Coupling Induced Valence Band Edge Shift in Mono- to Few-Layer MoS 2. *Scientific Reports* **2017**, *7*, 1–10.
73. Hilger, A.; Tenfelde, M.; Kreibig, U. Silver nanoparticles deposited on dielectric surfaces. *Applied Physics B: Lasers and Optics* **2001**, *73*, 361–372.
74. Berg, K.J.; Berger, A.; Hofmeister, H. Small silver particles in glass surface layers produced by sodium-silver ion exchange - their concentration and size depth profile. *Zeitschrift für Physik D Atoms, Molecules and Clusters* **1991**, *20*, 309–311.